Fiber-optic devices for sensing, manipulating, and imaging cells in vitro and in vivo

Shaodi Zhu, Shuwen Zeng, Yuye Wang, Aaron Ho Pui Ho, Wu Yuan

CHAPTER

11 Fiber-optic devices for sensing, manipulating, and imaging cells in vitro and in vivo

Shaodi Zhu[1,2,4], Shuwen Zeng[2,4], Yuye Wang[1,3], Ho-Pui Ho[1], Wu Yuan[1]

[1]Department of Biomedical Engineering, The Chinese University of Hong Kong, Shatin, New Territories, Hong Kong SAR, P.R. China; [2]CNRS, XLIM Research Institute, UMR 7252, University of Limoges, Limoges, France; [3]Laboratory of Biomedical Microsystems and Nano Devices, Bionic Sensing and Intelligence Center, Institute of Biomedical and Health Engineering, Shenzhen Institutes of Advanced Technology, Chinese Academy of Science, Shenzhen, P.R. China; [4]Light, Nanomaterials & Nanotechnologies (L2n), CNRS-ERL 7004, Université de Technologie de Troyes, Troyes, France

11.1 Introduction

The cell is the basic structural and functional unit of living organisms. Understanding the intracellular processes and the interaction between cells is essential for revealing the fundamental factors of physiological activities and pathogenic processes. Nowadays, available methods of cell analysis, i.e., characterizing the genotypes and phenotypes of living cells, are surging, accompanied by the recent advancements in biosensing and bioimaging technologies [1,2]. The mainstream analytical techniques include flow-cytometry-based cell sorting, fluorescent-labeling-assisted cell imaging, sequencing-based gene expression profiling, and mass-spectroscopy-based organic compound analysis [1].

Fiber optics has attracted increasing interest in the field of cell analysis since it possesses the advantages of compactness, flexibility, immunity to electromagnetic (EM) interference (EMI), and versatile application possibilities. For instance, the sub-millimeter scale diameter and the flexibility allow the fiber optics to propagate light into narrow spaces, which enables the remote cell analysis at almost arbitrary positions. In addition, the EMI immunity enables the fiber-optic analytical devices to be more stable during the operation in comparison with devices utilizing electric signals, such as electrochemical sensors. Moreover, the optical fiber can be further processed into various functional structures that make the light sensitive to surrounding refractive index (RI) or shape the output light, e.g., fiber gratings, interferometers, and focusing lenses [3]. The RI-sensitive structures can serve as highly

Microfluidic Biosensors. https://doi.org/10.1016/B978-0-12-823846-2.00019-5

sensitive label-free biosensors. The output shaping structures can serve as optical tweezers and endoscopes. These fiber-optic devices have been successfully utilized in various applications of cell analysis, such as biomarker detection [4–9], cell counting and/or sorting [10–13], and cell imaging [14–17].

This chapter will provide an overview of essential components for fiber-optic-based compact devices and their applications in cell sensing, manipulation, and imaging. To begin with, the basic principles of fiber-optic devices are introduced. Then, in vitro and in vivo applications of cell analysis in three scenarios are reviewed. For bulk-cell samples, both direct and indirect approaches to detecting specific cells and monitoring cell behaviors using fiber-optic biosensors are summarized. For single cells, cell/organelle manipulation and intracellular analysis with fiber-optic probes are introduced. For intravital cells, the in vivo cell detection in the circulation system and the minimally invasive cell imaging in deep tissues are presented.

11.2 Basic principles

This section will give a brief overview of utilizing structured fibers for cell analysis. These structured fibers are employed to perform two main functions: (1) transducing the environmental RI to spectral contents and phase, and (2) focusing the output beam to generate optical gradient force. Based on the functions, three analytical techniques will be introduced accordingly, i.e., plasmonic sensing, interferometric sensing, and optical trapping.

11.2.1 Plasmonic sensing

Plasmonic sensing is a commonly used mechanism of fiber-optic sensors [18–20]. The conventional plasmonic sensing configurations were established by Kretschmann and Otto on prisms [21,22]. The evanescent field from the total reflected incident beam can excite the collective oscillation of surface electrons in the adjacent metal film, which is also known as the surface plasmon polaritons (SPPs). Such surface plasmon resonance (SPR) would happen only if the wavenumber of the evanescent field (k_{ev}) equals the wavenumber of excited SPPs (k_{spp}), which is given as follows:

$$k_{ev} = \frac{2\pi}{\lambda} \sin\theta \sqrt{\varepsilon_p} \tag{11.1}$$

$$k_{spp} = \frac{2\pi}{\lambda} \sqrt{\frac{\varepsilon_m \varepsilon_d}{\varepsilon_m + \varepsilon_d}}. \tag{11.2}$$

In Eqs. (11.1) and (11.2), λ denotes the wavelength of the incident light, θ is the incident angle, and ε_p, ε_m, and ε_d are the relative electric permittivities of the glass prism, the metal film, and the dielectric analyte, respectively. Note that the RI, n, is commonly used in bioanalysis. As for nonmagnetic biomaterials, n equals $\sqrt{\varepsilon}$.

Therefore, the RI change of the analyte would result in a different k_{spp}, which matches a different k_{ev}. This manifests as the shift of SPR absorption angle θ when the incident light wavelength λ is fixed or the variation of absorption wavelength when a light beam of broad spectral bandwidth is incident at a certain angle θ.

Similar to SPR, localized SPR (LSPR) denotes that the excited collective oscillation of electrons is constrained in metallic nanoparticles. Unlike SPR, the excitation of oscillating electrons in nanoparticles does not require the exact matching of wavenumbers through an evanescent field [23]. For example, the resonance angular frequency ω_{LSPR} of spherical particles can be estimated using the following equation:

$$\omega_{LSPR} = \frac{\omega_p}{\sqrt{1 + 2\varepsilon_d}}. \tag{11.3}$$

The aforementioned equation is deduced from the Drude model [24], where ω_p and ε_d represent the plasma frequency of metallic nanoparticles and the relative permittivity of surrounding dielectrics, respectively. Note that ω_{LSPR} equals $2\pi c/\lambda$, with c being the speed of light in free space. Thus, the change of relative permittivity ε_d or refract index n would result in the shift of ω_{LSPR}, inducing the change of absorption wavelength λ.

It is worthwhile to mention that the local EM field of SPPs would be dramatically enhanced at resonance [8,23]. This enhanced EM field has been demonstrated to provide sensitivity amplification in conventional SPR sensing, fluorescence signals, and Raman scattering signals [25,26].

As for the fiber-optic-based plasmonic sensors (Fig. 11.1A), the unidimensional structure of optical fibers does not allow the convenient measurement of the incident angle of light, i.e., θ, as in the prism configurations. Hence, measuring the shift of absorption wavelength has become the mainstream interrogation approach [3,27,28]. As shown in Fig. 11.1B, a variety of fiber optic structures have been proposed for plasmonic sensing to achieve high sensitivity. These plasmonic sensors are implemented using different fiber techniques, including heterocore splicing [6,8,29], core exposing [9,30–32], side polishing [33], U-shaped bending [5,34], and fiber Bragg grating [4,35–37], to name a few.

11.2.2 Interferometric sensing

Fiber-optic-based interferometry is another widely used optical sensing technique. As illustrated in Fig. 11.2, a number of different optical fiber sensors have been proposed to enable a variety of interferometric technologies, such as the Fabry--Pérot interferometer(FPI), the Mach–Zehnder interferometer (MZI), the Michelson interferometer (MI), and the Sagnac interferometer (SI).

The FPI fiber sensors are usually fabricated by introducing an in-line optical cavity consisting of two closely spaced reflective surfaces into optical fiber through a fusion splicing procedure or other methods [39,40]. The RI change of the analyte

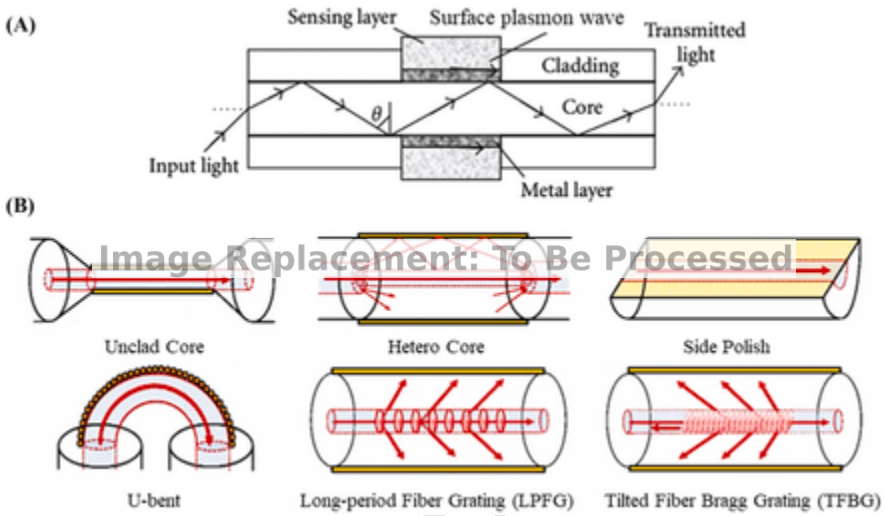

FIGURE 11.1

(A) Schematic showing the principle of the fiber-optic-based plasmonic sensor. (B) Typical fiber structures for plasmonic sensing.

within the cavity or attached to cavity walls will lead to a variation in the difference in optical path lengths (OPLs) between two light beams reflected from cavity surfaces, resulting in the shift of the peaks and valleys of the interference pattern.

The MZI fiber sensors split the propagation light in fiber into a reference beam and a sensing beam. The reference beam is usually confined in the fiber core, whereas the sensing beam will propagate in the fiber cladding region and interact with the ambient analyte. This type of fiber sensor can be fabricated through different methods, including fiber tapers, heterocore fiber splicing, and side polishing of optical fibers [7,41]. Since the OPL of the sensing beam is determined by the exposed cladding modes, which are sensitive to the RI of the surrounding analytes, the resulting peaks and valleys of the interference pattern will shift accordingly if the analytes' RI changes. Similar to the MZI counterparts, the MI fiber sensors also consist of reference and sensing beams. MI fiber sensors usually have a reflective mirror on the fiber end facet and measure the beam interference in the reflection mode [38,42]. In contrast, the MZI fiber sensors generally work in the transmission mode (Fig. 11.2).

The SI fiber sensors utilize a Sagnac loop, in which two orthogonal principal polarization states in the optical fiber are oppositely propagated as reference and sensing beams. The polarization states are tuned by a polarization controller, and the sensing part of the SI fiber consists of a polarization-maintaining fiber. The polarized sensing beam is exposed to surrounding analytes through etching or side

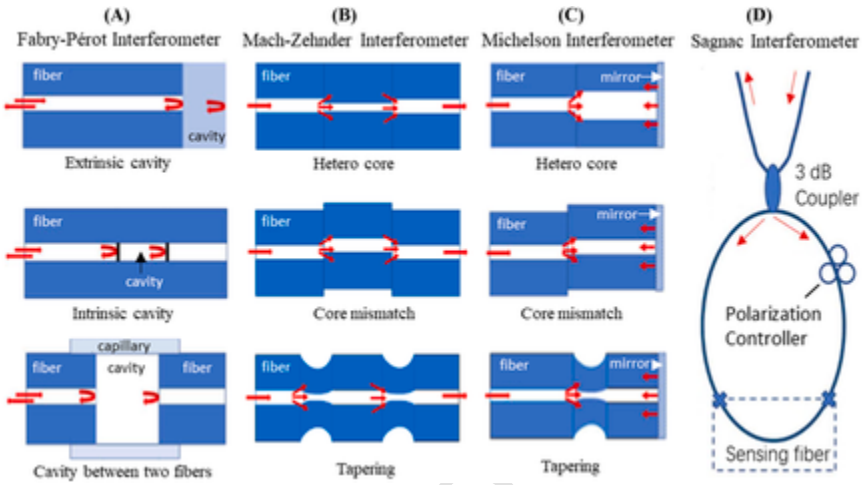

FIGURE 11.2

The typical fiber-optic-based interferometric sensing structures. (A) Fabry–Pérot interferometer (B) Mach-Zehnder interferometer (C) Michelson interferometer (D) Sagnac interferometer. Red arrows indicate the propagation direction of light [38].

- Adapted from [38]. *© 2021 the author.*

polishing of the optical fibers. The RI change of the analyte will only change the OPL of the polarized sensing beam and eventually lead to the shift of the peaks and valleys of the interference pattern between the polarized sensing and reference beams [43,44].

11.2.3 Optical cell trapping

The method of trapping particles using the optical gradient force of a tightly focused laser beam, also known as an optical tweezer, was established by Ashkin et al. [45]. As shown in Fig. 11.3A, the optical force on Rayleigh particles can be decomposed into an optical scattering force pushing the particle away and an optical gradient force induced by particle polarization toward focus [46]. Given the light intensity of I_0, the optical forces on a Rayleigh particle can be calculated using the following equations:

$$F_{\text{scat}} = \frac{\sigma n_{\text{m}}}{c} I_0 \tag{11.4}$$

$$F_{\text{grad}} = \frac{2\pi\alpha}{c n_{\text{m}}^2} \nabla I_0. \tag{11.5}$$

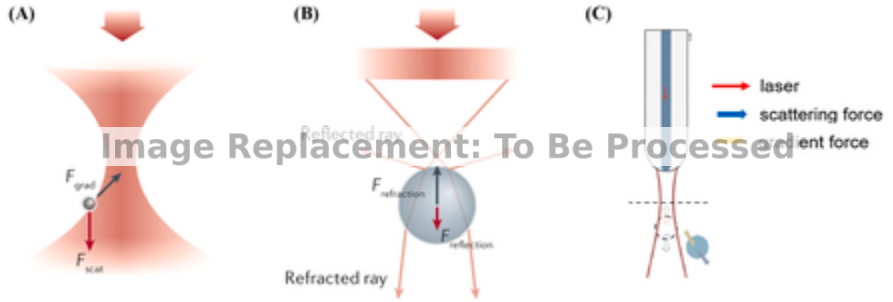

FIGURE 11.3

Schematics showing the optical trapping principle for (A) subwavelength Rayleigh particles and (B) cellular scale particles. . (C) Schematic of the optical fiber tweezer.

In Eqs. (11.4) and (11.5), σ is the scattering cross-section of a particle, α represents the polarizability of a particle, n_m denotes the RI of a particle, and c is the speed of light in free space. As for particles larger than the light wavelength or cellular-scale particles, the optical forces exerted by the tightly focused laser beam on cellular-scale particles can be simply interpreted using the reflective and refractive rays and their induced momentums on the particle. The refractive optical force pulls the particle/cell toward the focus, whereas the reflective optical force on the particle/cell surface leads to repulsion [48,49].

As for the fiber optical tweezer shown in Fig. 11.3C, the exerted optical forces on cells cannot be straightforwardly estimated using the above-mentioned ray method due to the loosely focused laser beam exiting from the fiber tip. In this case, electrodynamic simulation has been widely used to calculate the inhomogeneous distribution of the EM field and the resulting time-averaged Maxwell stress tension $\overline{T_M}$ on cells induced by the laser beam. Then, the total optical force on cells can be conveniently estimated using an integral of $\overline{T_M}$ over the cell surface S [47,50]

$$F_{\text{optical}} = \int \overline{T_M} \bullet \vec{n} \quad \mathrm{d}S \tag{11.6}$$

where $\vec{n}$ denotes the normal vector on the cell surface [50,51].

As for fiber-optic-based cell imaging, a variety of working principles have been successfully implemented, and the selected cases will be introduced in Section 11.5.2.

11.3 Bulk-cell analysis

The bulk-cell analysis in this chapter refers to the analytical measurement of the common properties in a sample containing a large number of cells. The bulk-cell sample can be obtained by culturing cells or processing biopsy samples. Three properties can be measured by fiber-optic biosensors in this scenario. The first is the number of cells that express specific membrane markers [4–6]. Their membrane marker expression level can also be measured accordingly [5,6]. The second is the concentration of cell metabolites, such as nucleotides [7], proteins [8], and extracellular vesicles (EVs) [9]. The third is the cell responses against environmental stimuli, such as the antigen-induced mast cell activation [30,35], as well as the fetal bovine serum (FBS)-induced nutrient uptake, sodium-azide-induced metabolism inhibition, and trypsin-induced cell detachment [35].

Recently, various fiber-optic biosensors have been proposed to provide a highly sensitive, label-free, and real-time approach for detecting specific cells and profiling their metabolites and responses. Thanks to their unique advantages of compact size and one-step-detection capability, they have become competitive choices in clinical applications, especially for point-of-care testing.

11.3.1 Detecting cell

Cell detection using fiber optics is typically an affinity assay targeting the biomarkers expressed on the cell membrane. Accordingly, it can also serve as an approach to measure the membrane biomarker expression level. The detection of mutated cells in bulk samples, such as blood and single-cell suspension, plays a crucial role in cancer diagnostics. For example, the presence of circulating tumor cells (CTCs) in blood shedding from solid tumors is believed to be associated with hematogenous metastasis. Therefore, it can be used as a biomarker to determine the progression of cancer. Moreover, the membrane biomarker expression level, such as *N*-glycan expression for glucose transporters (GLUTs), can be used as an indicator for monitoring the growth of different cancer cells after incubation with the external stimuli of inhibitors.

Loyez et al. proposed an aptamer-functionalized tilted fiber Bragg grating SPR (TFBG-SPR) fiber sensor for detecting breast-originated CTCs [4]. As shown in Fig. 11.4, the sensor was fabricated by coating a 50-nm-thick gold film on TFBG and subsequently functionalized by MAMA2 aptamers. These aptamers are short oligonucleotides with a high affinity toward mammaglobin (MAM) on the MDA-MB-415 cell line [52]. Besides, the aptamer-functionalized sensor also showed significant specificity in the control experiments of MAM-negative cells. Furthermore, this work demonstrated the nonlabel CTC detection limit in phosphate-buffered saline (PBS) at 49 cells/mL, by measuring the extinction spectrum of the most sensitive SPR mode. In addition, the experimental limit of detection (LOD) can be fur-

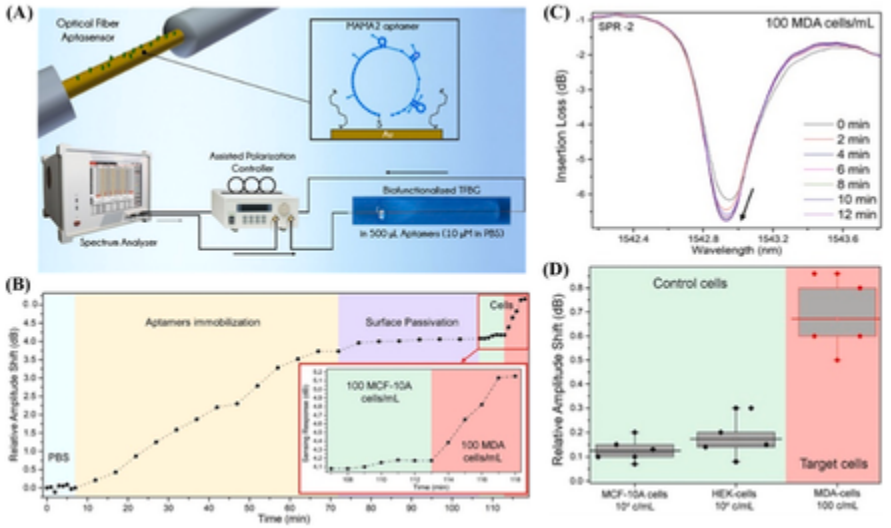

FIGURE 11.4

(A) Optical interrogation setup for the TFBG-SPR cytosensor and the schematic of sensor functionalization. (B) Sensorgram during the functionalization, blocking, and cell detection. The analysis was performed in phosphate-buffered saline (PBS). (C) Extinction spectra of an SPR-sensitive mode acquired during a 12-minute binding process of the target cell. (D) Boxplots of the biosensing shifts between the control and the target. *TFBG-SPR*, Tilted fiber Bragg grating surface plasmon resonance.

- Adapted with permission from [4]. *© 2020 American Chemical Society.*

ther reduced to 10 cells/mL by using aptamer-functionalized gold nanoparticles (AuNPs) of 10 nm in diameter.

The combination of cytosensing and evaluation of membrane marker expression has also attracted academic interest. Luo et al. proposed a cytosensing system based on a U-shaped LSPR fiber sensor with concanavalin A functionalization [5]. As displayed in Fig. 11.5, the sensor was fabricated through the cladding etching and U-bending of a fiber with a 600-µm core. A layer of AuNPs was subsequently coated. The RI sensitivity was optimized by adjusting the outer bending diameter to 4 mm and the AuNPs' size to 32 nm.

The detection of MDA-MB-231 cancer cells has been demonstrated through the affinity binding between *N*-glycan and concanavalin A. The calculated LOD of the optimized sensor was 30 cells/mL. Furthermore, the authors also examined the *N*-glycan expression level on six different cell lines through tunicamycin (TM) inhibitor treatment. The resulting LSPR absorption is proportional to the *N*-glycan expression level and would progressively decrease with the increased concentration of TM, suggesting the sensor as a promising tool to study *N*-glycan-related biological processes.

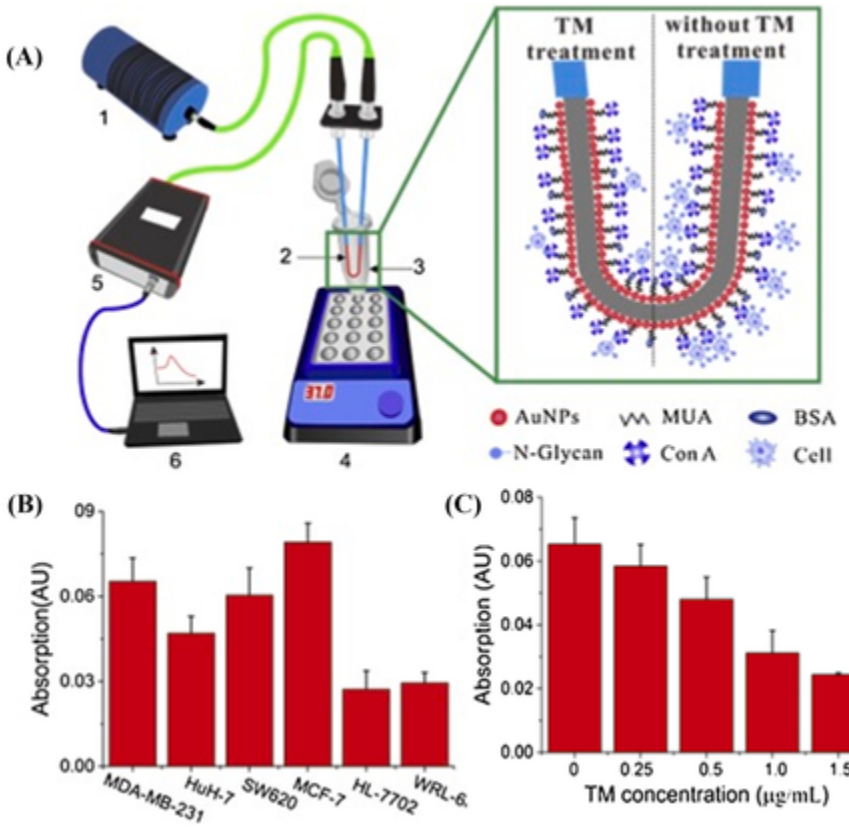

FIGURE 11.5

(A) Experimental setup for a U-shaped fiber-optic cytosensor and schematic of sensor functionalization. (B) LSPR absorption across different cells, cell suspension concentration 1×10^5 cells/mL. (C) LSPR absorption versus TM concentration. Cell line MDA-MB-231, concentration 1×10^5 cells/mL. *LSPR*, Localized surface plasmon resonance; *TM*, tunicamycin. *Adapted with permission from* [5]. © 2019 Elsevier

Apart from the transmissive optical interrogation configurations mentioned above, several fiber-optic biosensors adopted a reflective design [6,9,30]. Singh et al. proposed a heterocore reflective LSPR cytosensor by splicing a 1-mm etched multicore fiber (MCF) into a single-mode fiber (SMF) [6]. The sensing layer was composed of sequentially coated graphene oxide (GO), AuNPs, and copper oxide nanoflowers (CuO-NFs) (Fig. 11.6A). In this design, the GO and CuO-NFs were reported to enhance surface biocompatibility [53,54], and AuNPs were regularly employed as LSPR sensing agents. Moreover, the biosensor was further functionalized by 2-deoxy-D-glucose targeting GLUTs overexpressed on cancer cells. Based

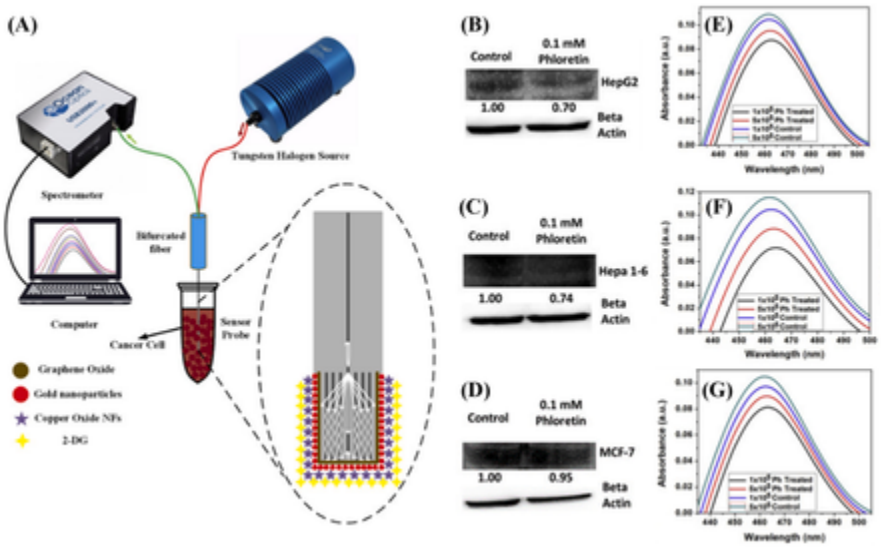

FIGURE 11.6

(A) Experimental setup and the schematic of probe functionalization of the heterocore reflective LSPR cytosensor. (B–D) Western blot showing GLUT expression between control and 0.1 mM phloretin inhibitor treated cancer cell lines. (E–G) LSPR absorption spectra at different cell concentrations (cells/mL). Cell lines: (B and E) HePG2, (C, F) Hepa1-6, and (D, G) MCF-7. *LSPR*, Localized surface plasmon resonance; *GLUT*, glucose transporter.

- Adapted with permission from [6]. *© 2020 Elsevier.*

on such affinity, the authors demonstrated the cytosensing of four different cancer cell lines, i.e., Hepa1-6, A549, MCF-7, and HepG. The calculated LODs were 2, 2, 2, and 3 cells/mL, respectively. Similar to the work of Luo et al. [5], the correlation between the GLUT expression level and LSPR absorption has also been confirmed in this work (Fig. 11.6B–G).

11.3.2 Detecting cell metabolites

Cell metabolites, such as nucleic acids, proteins, and EVs, are also important biomarkers for profiling specific cells. The metabolites are released into the blood, saliva, urine, or other body fluids through exocytosis and apoptosis, carrying the metabolic and genomic information of cells.

Lu et al. proposed a AuNP-enhanced MZI sensor for nucleic acid detection [7]. The microfiber was fabricated by tapering the SMF, as shown in Fig. 11.7. The taper region allows for the excitation of higher-order modes and the recombination with core modes to form interference. Since the surrounding RI strongly influences the phase of higher-order modes propagating along the fiber cladding, the RI

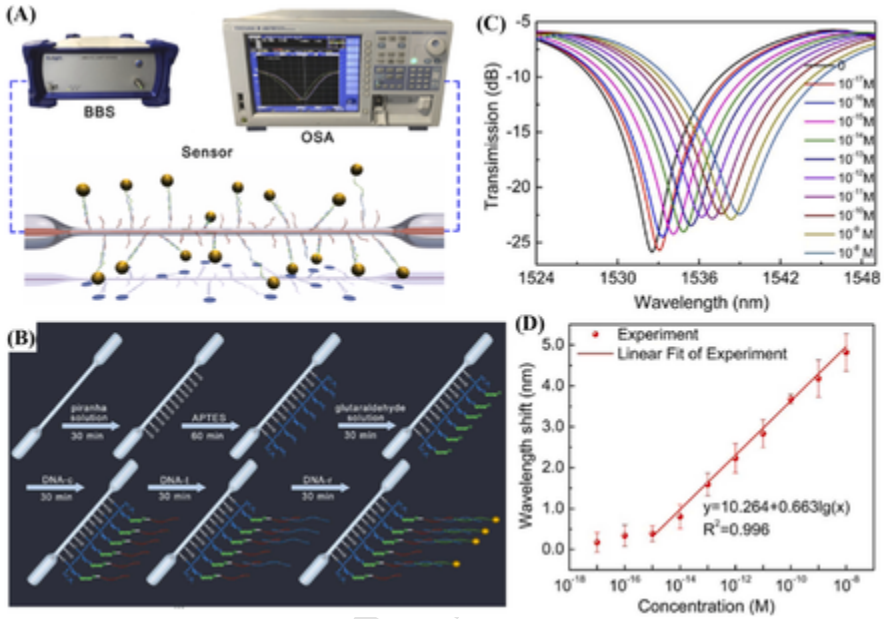

FIGURE 11.7

(A) Schematic of the experimental setup and surface functionalization of the MZI microfiber sensor. (B) Schematic of functionalization and DNA hybridization process. (C) Transmission spectra of DNA-t hybridization with AuNP amplification. (D) The shift of the dip wavelength versus DNA-t concentration. *MZI*, Mach–Zehnder interferometer.

- Adapted from [7]. *© 2021 Optical Society of America under the terms of the OSA Open Access.*

change can result in an interference shift [55,56]. The authors functionalized the microfiber with a predesigned oligo sequence for targeted capture and employed a complementary oligo decorated with AuNPs for signal amplification, also known as the "sandwich" configuration [57]. In this work, the authors improved the detection limit of oligos to the order of 10^{-15} M and showed excellent selectivity against the mismatched oligo sequences.

Xia et al. reported another approach of combining plasmonic nanoparticles and the RI sensor for label-free and ultrasensitive immunoassay [8]. They proposed that the stacking of nanoparticles with nanorods can enhance the EM field of LSPR and improve the sensitivity of immunoassay. As shown in Fig. 11.8, a heterocore sensor was developed by coating a layer of 50-nm gold and two additional layers of gold particles and nanorods on a photonic crystal fiber. A sensitivity of 25,642 nm/RIU was identified by measuring solutions of different refractive indices. Furthermore, the immunosensing performance was evaluated by further functionalizing the sensor with GO and Immunoglobuline G (IgG) antibodies. The LOD of human IgG is 4.6 ng/mL, which is in the order of 10^{-11} M [58].

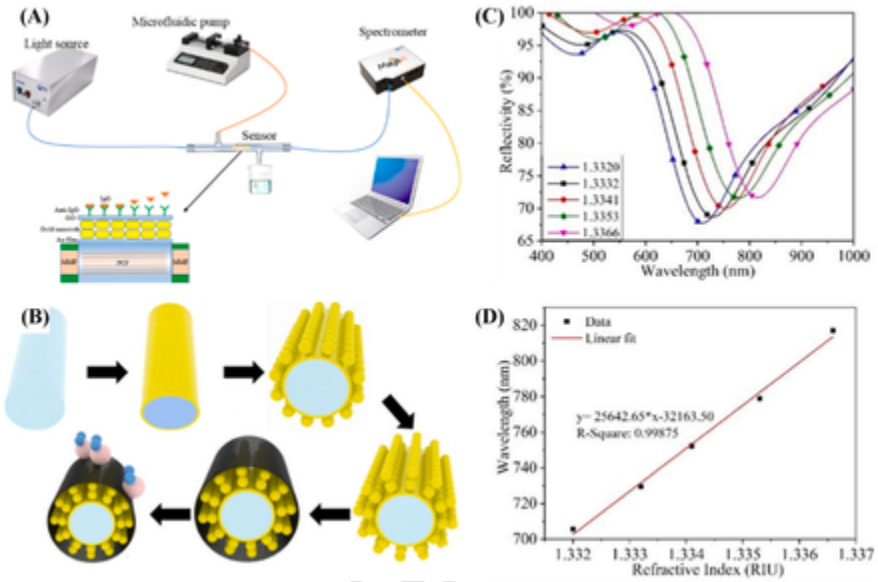

FIGURE 11.8

(A) Schematic of the immunoassay setup. (B) Flowchart showing the fabrication of nanoparticles–nanorods sensor. Note that the nanoparticles are not in scale for clarity. (C) LSPR spectra of the nanorod immobilized sensor in different refractive solutions. (D) The sensitivity of the nanorod immobilized sensor. *LSPR*, Localized surface plasmon resonance.

- Adapted with permission from [8]. *© 2020 Elsevier.*

In addition to biomolecules, larger metabolites, like EVs, are easier to be detected with an RI sensor. Yildizhan et al. reported a novel EV detection approach with a commercialized fiber-optic SPR probing system [9] (Fox Biosystems Inc.). This work explored the target enrichment and detection with different antibodies to selectively maximize the signal of EVs from specific cancer cells, as shown in Fig. 11.9. Through recombinant sample calibration, the LOD of EVs in complex matrices, such as plasma and cell culture medium, is in the order of 10^7 counts/mL, which is 10^4 times lower than the concentration in a typical cancer patient's plasma [59].

11.3.3 Monitoring cell behavior

Other than detecting membrane markers and metabolites of cells, fiber-optic sensors have also been used to study cell behaviors against stimuli through detecting the subtle RI change. For example, Yanase et al. proposed an SPR fiber optic sensor to detect the antigen-induced activation of mast cells [30]. The sensor was fabricated by coating a 50-nm gold sensing layer on an exposed fiber of 200 μm in di-

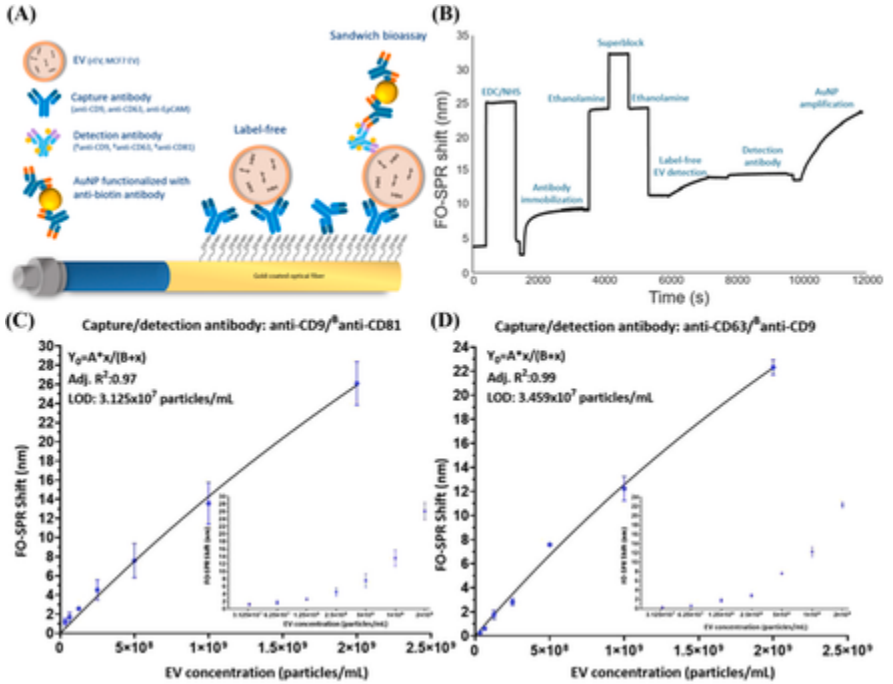

FIGURE 11.9

(A) Schematic of surface functionalization and EV-targeted immunoassay. (B) SPR dip wavelength shift during the immunoassay. (C, D) SPR dip wavelength shift versus EV concentration when using different detection antibodies. *SPR*, Surface plasmon resonance.

- Adapted from [9]. *© 2021 the authors.*

ameter. Moreover, an aluminum layer coated on the fiber tip allows for the interrogation of the reflected signal. The RBL-2H3 mast cells can be immobilized on the sensor surface with biotin functionalization. As shown in Fig. 11.10, through dinitrophenol (DNP) antibody sensitization, the authors have demonstrated in situ detection of the cellular immune reaction induced by DNP-conjugated human serum albumin [60].

As shown in Fig. 11.11, Shevchenko et al. reported another cell behavior monitoring platform based on a TFBG-SPR fiber sensor [35]. In this work, the intensity of the SPR signal was proportional to the ambient RI, which consists of the contributions from the background medium and the density and morphology of cells attached to the sensing fiber. Therefore, with rigorously controlled experiments, cell behaviors can be recognized from the change of the SPR signal and RI. The authors examined the fibronectin immobilized NIH-3T3 fibroblast under various stimuli and confirmed the RI change resulting from the cell activities, including FBS up-

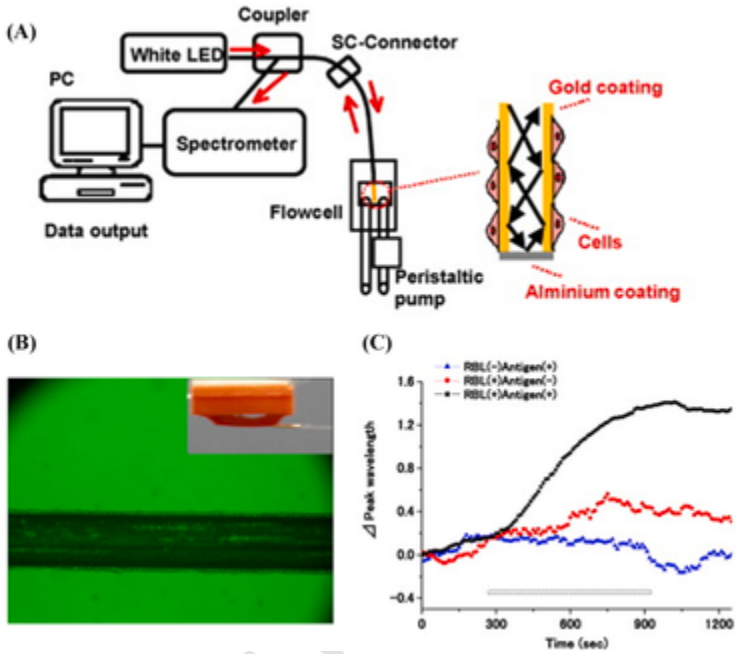

FIGURE 11.10

(A) Optical interrogation setup and the schematic of the probe structure for monitoring the cell's responses to stimuli. (B) An image of the immobilized mast cells on the fiber surface acquired with a phase-contrast microscope. (C) Refractive indices change of DNP-IgE activated (+) and inactivated (−) RBL-2H3 cells with DNP-conjugated human serum albumin stimulation.

- Adapted with permission from [30]. *© 2010 Elsevier.*

take, trypsin-induced detachment, and sodium-azide-induced metabolism inhibition.

11.4 Single-cell analysis

The single-cell analysis includes the studies of genomics, transcriptomics, proteomics, metabolomics, and cell–cell interactions on individual cells [2], which can provide valuable information on intracellular biological dynamics and the cell-to-cell variation within a cell population [61]. Fiber-tip-based manipulation by optical gradient force [10,62,63] and fiber-optic intracellular sensing [31,32,36] are important analytical techniques in this scenario and provide the needed flexibility and multifunctionality for evaluating the mechanical and biological properties of the cell.

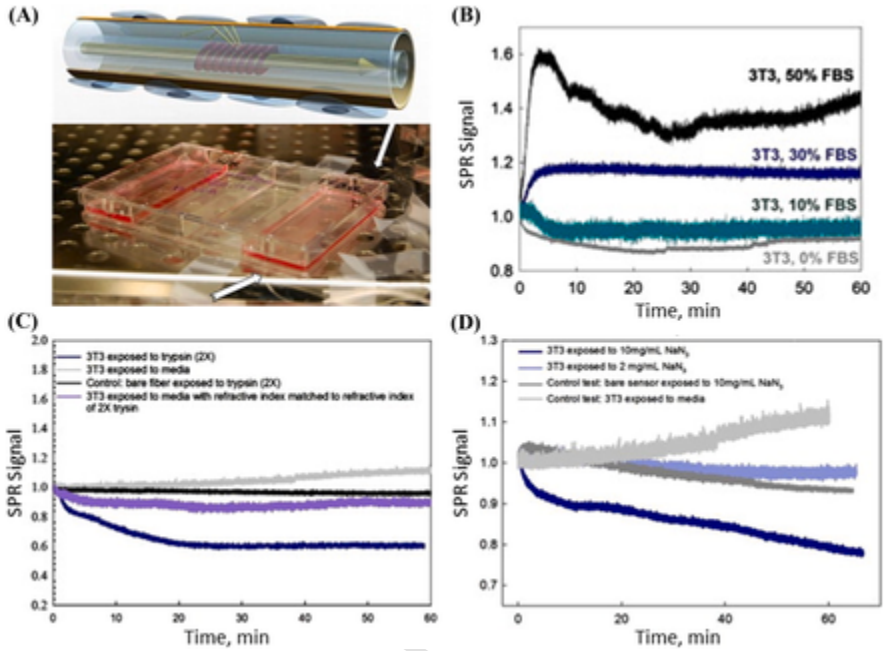

FIGURE 11.11

(A) Schematic of the proposed TFBG-SPR fiber sensor and the picture showing the sensing setup. (B) SPR signal monitoring the cellular uptake of FBS. (C) SPR signal of cell detachment through trypsin. (D) SPR signal monitoring the cellular metabolism inhibition through sodium azide. *FBS*, Fetal bovine serum; *TFBG-SPR*, tilted fiber Bragg grating surface plasmon resonance.

- Adapted with permission from [35]. *© 2014 Elsevier.*

11.4.1 Manipulating cells and organelles

There are three types of single-cell analysis based on cellular and subcellular manipulation. The first type is to position and sort cells and organelles based on a templated assembly process. The second type is to measure the mechanical properties at cellular and subcellular levels, such as the velocity of organelle movement and the power of molecular motors. The third type is to perform a microsurgery and realize the gene delivery into the cell.

Liu et al. proposed an optical fiber tweezer (OFT)-based cell sorting chip for selectively separating *Escherichia coli* cells from red blood cells (RBCs) by leveraging their difference in morphology [10]. A tapered fiber tip (Fig. 11.12) was designed to generate the proper optical gradient force distribution for trapping *E. coli* while pushing the RBCs away. By using a 1064-nm laser of 10 mW, the authors

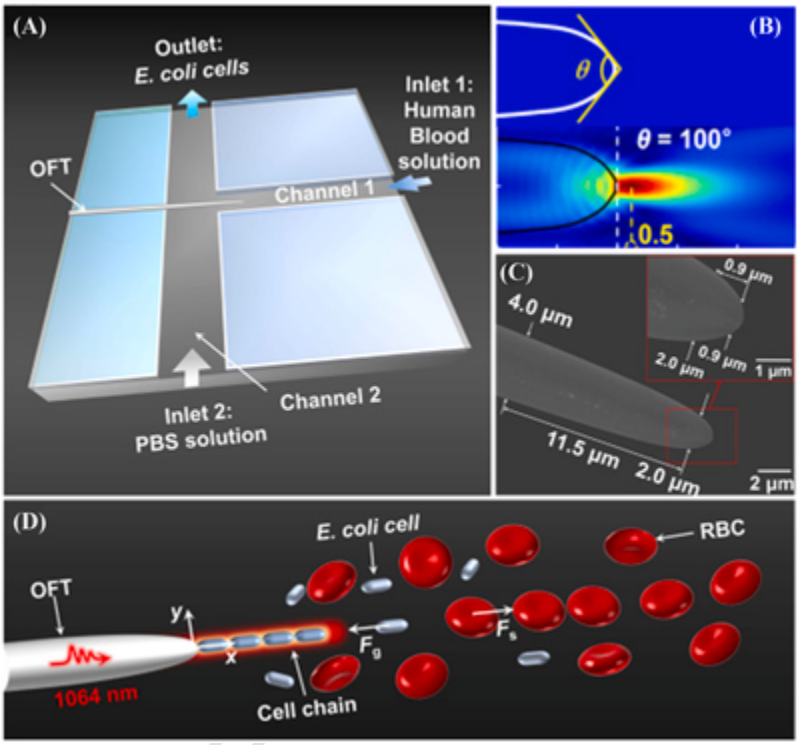

FIGURE 11.12

(A) Schematic of the OFT-based cell sorting setup. (B) Numerical simulation of electromagnetic field on the fiber tip. (C) Scanning electron microscopy (SEM) picture of the fiber tip. (D) Artistic illustration of using OFT to separate *E. coli* cells from RBCs. *OFT*, Optical fiber tweezer; *RBCs*, red blood cells.

- Adapted with permission from [10]. *© 2019 Optical Society of America.*

have demonstrated the capability of trapping *E. coli* cells in a 20 μm/s dynamic flow with a trapping distance of less than 8.8 μm. More interestingly, *E. coli* cells can be further arranged in a cell chain on a fiber tip and the length can be extended with a higher laser power [64]. In addition to *E. coli*, the authors have also discussed the feasibility of cancer cell separation through simulation, showing the versatility of the OFT sorting technique.

Li et al. reported the operation of OFT at the subcellular scale [62]. Different from the work of Liu et al. [10], the fiber tip was designed to deliver the trapping center further away from the fiber tip to offer a noncontact in vivo manipulation force (Fig. 11.13). The authors have demonstrated the moving and arranging of chloroplasts on *Hydrilla verticillata* leaves by launching a 980-nm laser with an optical power of 20–50 mW. The maximum velocity of intracellular chloroplasts

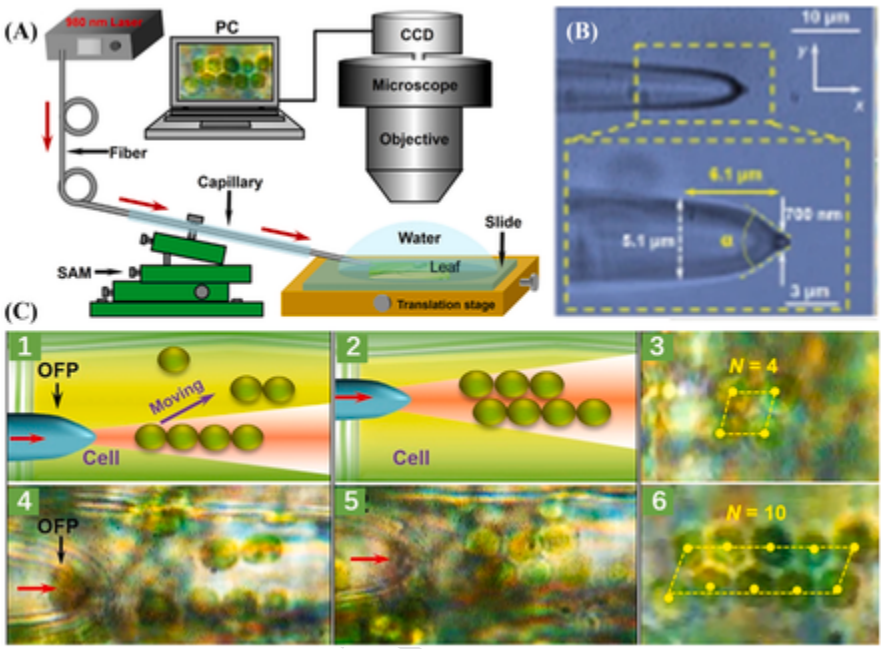

FIGURE 11.13

(A) Schematic of the experimental setup of OFT. (B) Microscopy picture showing the details of the fiber tip. (C) Schematic and pictures of binding multiple chloroplasts. *OFT*, Optical fiber tweezer.

- Adapted from [62]. *© 2015 the authors.*

transported by OFT is 7.5 ± 0.2 μm/s at 35 mW power output. This work has further explored the cytoplasmic viscosity measurement to indicate the integrity of the cell matrix.

Zhao et al. further widened the application of OFT in subcellular operation [63]. They proposed a technique that combined thermoplastics and optical trapping for in situ intracellular organelle manipulation and single-cell microsurgery (Fig. 11.14). In this work, the photothermal effect from internalized gold nanorods was demonstrated to induce localized breakdown and repair of the cell membrane. With an 808-nm laser of 15 mW and a 5-minute irradiation, the perforated hole size was found to be 8.7 μm. Higher optical power and longer irradiation time will result in larger wound size and potential intracellular damage, whereas a lower power of less than 14 mW will lead to a wound that can be repaired by a heat-facilitated Brownian diffusion reversely. The authors have demonstrated the mitochondrial extraction from cells with minor damage.

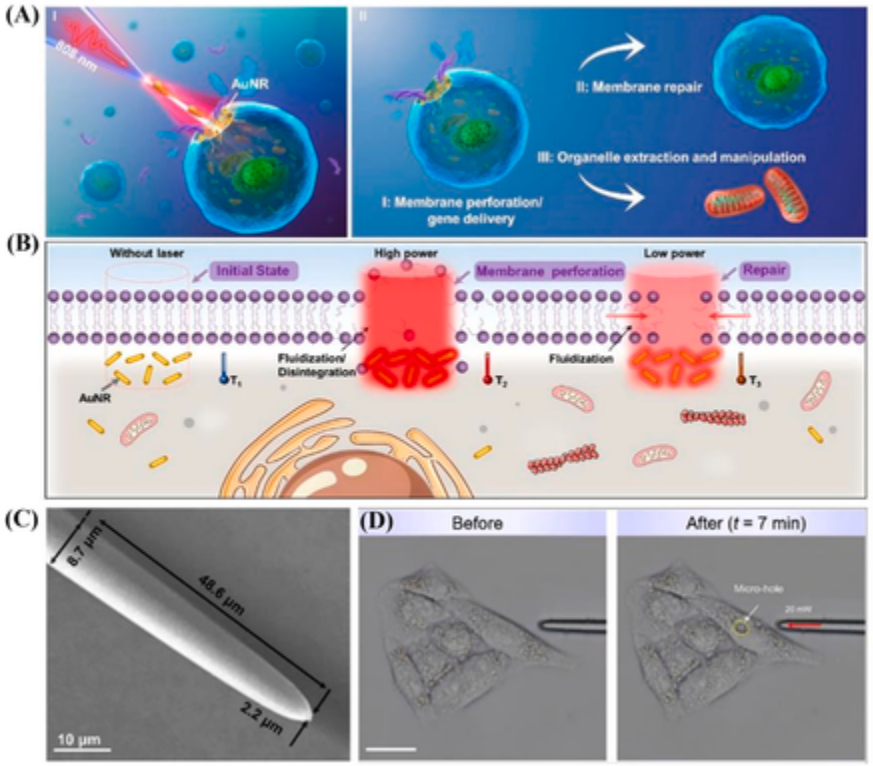

FIGURE 11.14

(A) Artistic illustration of the microsurgery process on the cell. (B) Schematic of membrane perforating and repairing of the cell. (C) Scanning electron microscope (SEM) picture showing the fiber tip details. (D) Microscopy picture of cell membrane perforation.

- Adapted with permission from [63]. *© 2022 American Chemical Society.*

11.4.2 Probing intracellular process

In addition to the optical tweezers implemented on fiber tips, nanoscale fiber tip bioprobes are also emerging in recent years. These probes opened a precise window for understanding intracellular dynamics, such as the protein uptake [31], oxidative stress [32], and apoptosis [36]. For example, Hong et al. proposed a label-free LSPR sensor on fiber tip for protein uptake analysis [31]. The fiber tip was fabricated with a precisely monitored wet etching process, which can help achieve a tip of a diameter less than 100 nm, minimizing the invasiveness in cell. A gold nanorod as an LSPR agent was sequentially picked from a dispersion droplet and attached to the fiber tip. The authors have demonstrated the detection of tumor suppressor pro-

tein p53 with sc-126 antibody functionalization. The resulting LOD was less than 1 nM. Using this probe, the p53 uptake process in HeLa cells has been investigated under various therapeutic stimuli, such as UV radiation and neocarzinostatin exposure (Fig. 11.15).

The cellular oxidative stress induced by reactive oxygen species (ROS) has also been explored for many years since the intracellular redox process can help reveal the key factors of aging and metabolic diseases [65,66]. Chen et al. reported a fiber-tip-based surface-enhanced Raman spectroscopy (SERS) sensor for intracellular monitoring of ROS and the reduced form of nicotinamide adenine dinucleotide (NADH) [32]. The sensor was fabricated through a wet etching method similar to that used by Hong et al. [31], except that silver nanoparticles were sequentially deposited as an SERS substrate in this work. The authors have examined the cellular response with oxidative stress inducer phorbol 12-myristate 13-acetate and demonstrated the oxidation events from ROS generation as well as the reduction from NADH. This process has been monitored through the transform between Raman active 4-mercaptophenol and Raman inactive 4-mercaptocyclohexa-2,5-dienone functionalized on the fiber tip (Fig. 11.16).

For single-cell analysis, the necessity of a high-quality microscopic device for signal collection has limited the in vivo detection in deep tissues. Recently, Li et al have reported an all-fiber subcellular sensor for intracellular RI sensing, as shown in Fig. 11.17 [36]. The sensor was fabricated by integrating a zinc oxide (ZnO) nanograting onto a fiber taper tip. Light coupled in ZnO nanograting will be partially reflected (~30% at 655 nm), and the central wavelength of the reflected spec-

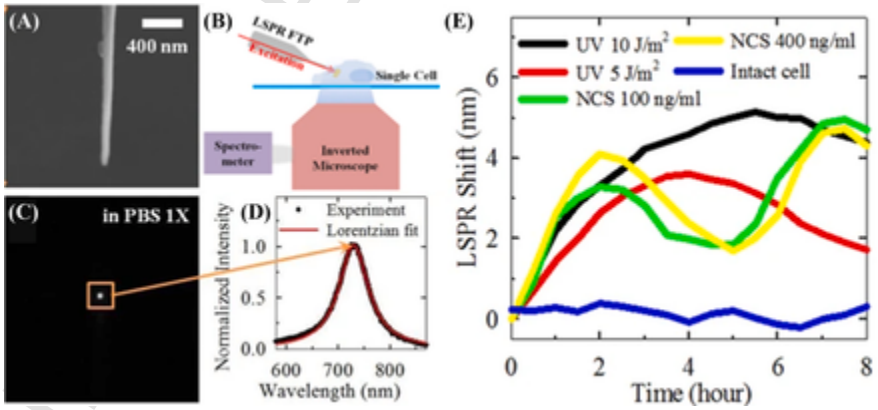

FIGURE 11.15

(A) Scanning electron microscope (SEM) picture of the nanoscale fiber tip with a gold nanorod attached. (B) The experimental setup for intracellular sensing. (C) Microscopic picture showing the scattering from the fiber tip. (D) The spectrum of the scattered light. (E) LSPR spectra shift illustrating the p53 dynamic in HeLa cells. *LSPR*, Localized surface plasmon resonance.

- Adapted from [31]. *© 2014 the authors.*

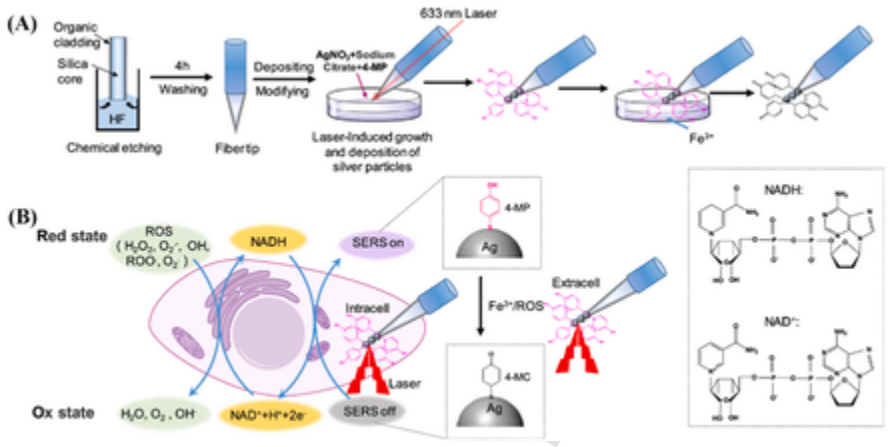

FIGURE 11.16

(A) Schematic of fabricating the fiber tip SERS sensor. (B) Schematics showing the principle of intracellular redox reaction detection. *SERS*, Surface-enhanced Raman spectroscopy.

- Reproduced with permission from [32]. *© 2021 American Chemical Society.*

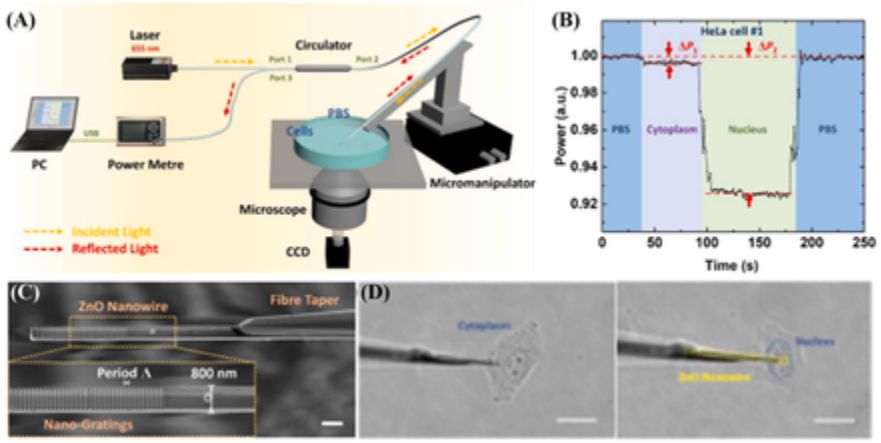

FIGURE 11.17

(A) Schematic of the experimental setup. (B) Reflection intensity showing the intracellular RI difference. (C) Details of ZnO nanograting attached on the tapered optical fiber. (D) Pictures of intracellular RI sensing.

- Adapted from [36]. *© 2022 the authors.*

trum was determined by the surrounding RI. The diameter of nanograting is 800 nm, which would significantly reduce the damage to cells. The authors have investigated the intracellular RI of HeLa cells and demonstrated the RI change of the nucleus during apoptosis.

11.5 Intravital-cell analysis

The flexibility and low profile of optical fibers enable the successful translation of a bulky microscopy system to a miniaturized fiber optic imaging device [67–71]. In vivo flow cytometry and endomicroscopy are the most widely adopted techniques for fiber-based intravital-cell analysis. In vivo flow cytometry provides rapid cell screening in the circulation system, whereas endomicroscopy offers morphological and physiological details of cells in tissues.

11.5.1 In vivo flow cytometry

In vivo flow cytometry was first proposed by Georgakoudi et al. in 2004 to introduce a new cell counting approach through an intravital fluorescent microscope [72]. After that, a variety of techniques have been developed in this field as an important preclinical research tool [73]. For instance, Pera et al. reported a multimode-fiber-bundle-based in vivo cytometry for detecting scattered fluorescence from labeled CTCs, named diffuse fluorescence flow cytometer (DFFC) [11]. The fiber probe is composed of a central fiber delivering an excitation laser beam through a 635-nm bandpass filter and eight surrounding fibers for collecting fluorescent signals through 650-nm long-pass filters. The backscattered fluorescent signals from the labeled CTCs in superficial blood vessels were then detected by photomultiplier tube (PMT) and indicated as intensity spikes during the continuous recording of DFFC. The detection of multiple circulating myeloma cells has been demonstrated in the tails of nude mice; the count rate was found to be roughly proportional to the concentration of the injected CTCs.

Recently, the same group has introduced a dual-probe DFFC configuration to further enhance the sensitivity, reduce false-positive signals, and improve the penetration depth (~2 mm) in tissues, as shown in Fig. 11.18 [12]. The dual probe was placed along the paired ventral caudal artery and vein, where the labeled CTCs traveled in the opposite direction. There, the cell passing event can be detected as a matched peak pair to remove the random fluorescent signal. The consistent flow speed of cells allowed the convenient conversion of the count rate to the CTC concentration. The false alarm rate from the control sample was found to be 0.014 count/min, indicating a detection limit of 0.35 cells/mL.

Despite the wide applications of fluorescent dyes in animal models, their safety issues in clinical applications require further study. Hence, label-free modality, such as photoacoustic (PA) technology, has attracted great interest. Juratli et al. proposed an acoustic-resolution PA probe for detecting the formation of intravascular blood cell emboli (Fig. 11.19) [13], which is also known as circulating blood clots

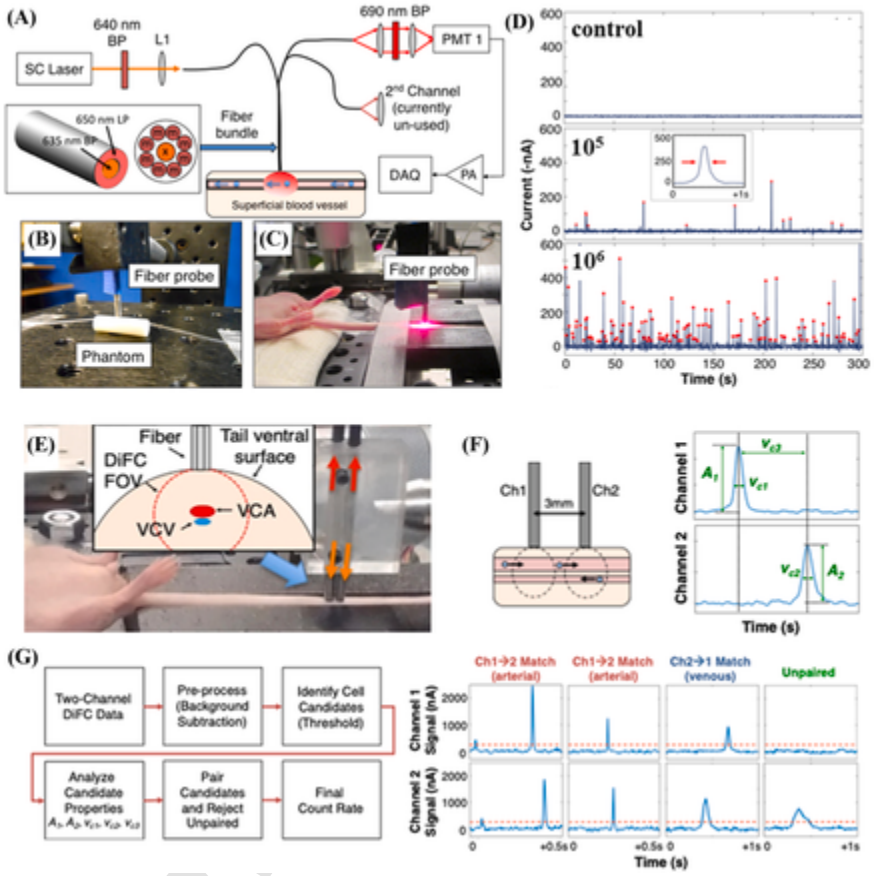

FIGURE 11.18

(A) Schematic of the DFFC system. The detection in flow phantom (B) and on mouse tail (C). (D) Data trace from mice injected with 10^5 and 10^6 cancer cells. The intensity peaks indicate the fluorescently labeled passing tumor cells. (E) Dual-probe DFFC system. (F) Cell passing event detected by two channels. (G) Dual-probe cell detection algorithm. *DFFC*, Diffuse fluorescence flow cytometer.

- (A–D) Adapted from [11]. *© 2017 the authors. (E–G) Adapted from* [12]. *© 2019 the authors.*

(CBCs). Using a 1064-nm laser, the selective absorption of hemoglobin would provide a stable ultrasound signal, which was detected by a transducer focusing inside the blood vessel (with a resolution 45–80 μm). If a high-absorptive erythrocyte-rich CBC or a low-absorptive leukocytes/ platelet-rich CBC passes by, different absorption properties will result in a positive or negative peak, respectively, while the CBC with mixed cells generate a combined contrast. The authors have examined the vessel injury induced coagulation and demonstrated the detection of emboli

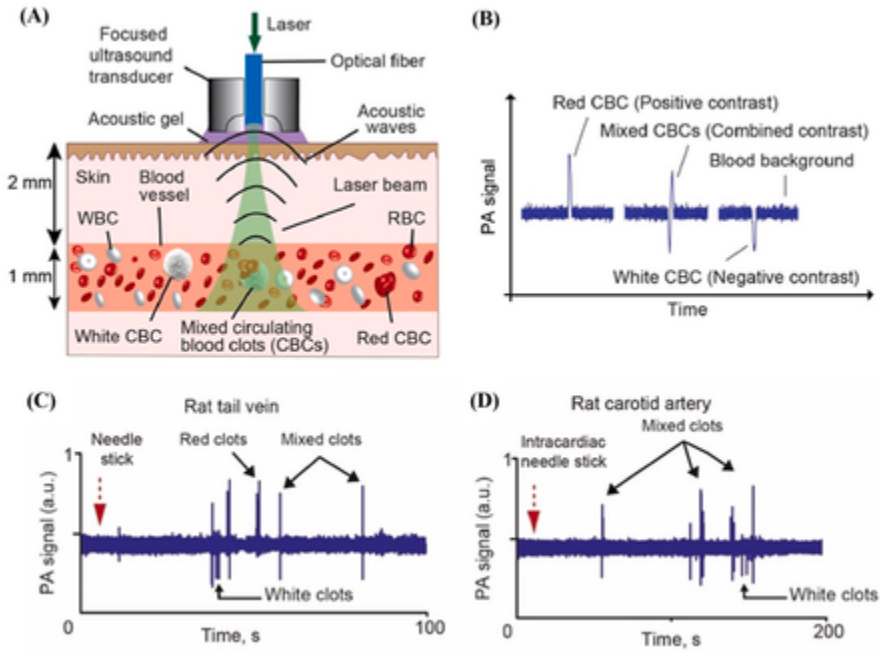

FIGURE 11.19

(A) Schematic of PA probe for CBC detection. (B) Data trace of different types of CBCs. The blood vessel injury induced CBC forming in (C) rat tail vein and (D) carotid artery. *CBC*, Circulating blood clots; *PA*, photoacoustic.

- Adapted from [13]. *© 2018 Optical Society of America under the terms of the OSA Open Access Publishing Agreement.*

generation in both rat tail vein (depth 0.3 mm) and carotid artery (depth 3–4 mm). Their previous work has also demonstrated the detection of embolus with an optical-resolution PA, which provided a higher resolution and a shallower penetration depth of 0.1–0.15 mm [74].

11.5.2 Endomicroscopy

In contrast to the single-point detection of in vivo flow cytometry, endomicroscopy performs in vivo tissue imaging with a cellular resolution and a large field of view. The temporal resolution of endomicroscopy is usually lower than that of in vivo flow cytometry. Such a modality fills the gap between 2D histological analysis and 3D pathological imaging of magnetic resonance imaging (MRI), computerized tomography (CT), and ultrasound imaging.

Typical endomicroscopy has been modified from the conventional microscopy through minimizing and fiberizing the bulky optics [14–16]. Liang et al. reported a

compact nonlinear endomicroscopy probe of ~2 mm in diameter, offering a subcellular resolution of ~0.7 μm in the lateral direction and ~6.5 μm in the axial direction [16]. This probe was composed of a miniature objective lens and a customized double-clad fiber driven by a piezoelectric scanner, providing a working distance of 200 μm. The laser transmitted in the fiber core was used to excite nonlinear signals of tissue, including two-photon fluorescence and second harmonic scattering, which were subsequently collected back into the inner cladding of the fiber. As illustrated in Fig. 11.20, the nonlinear endomicroscopic images clearly delineated the subcellular structure and extracellular matrix of mouse tissues both in vitro and in vivo. As a label-free imaging modality, this probe has great clinical potential for in situ optical biopsy.

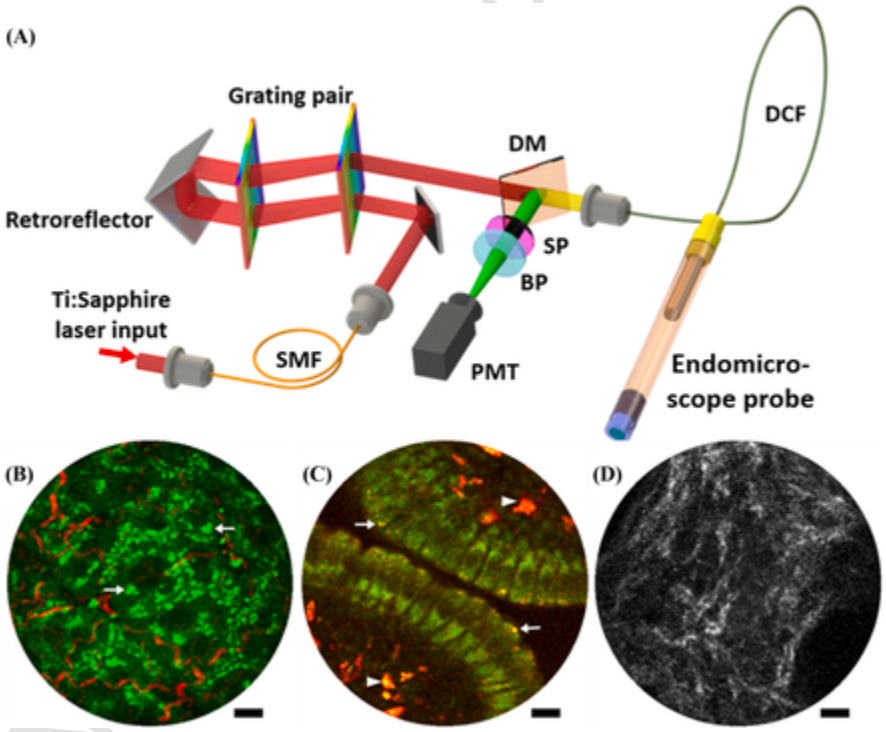

FIGURE 11.20

(A) Schematic of the experimental setup of two-photon endomicroscopy. (B) In vitro imaging of the mouse liver overlapping 2PF (green) with SHG (red). (C) In vivo 2PF image of autofluorescence of NADH (green) and Flavin adenine dinucleotide (FAD, red) from the mucosa of the mouse small intestine. (D) In vitro SHG image of the mouse cervical collagen fiber network. *2PF*, Two-photon fluorescent; *NADH*, nicotinamide adenine dinucleotide; *SHG*, second-harmonic generation signal.

- Adapted from [16]. *© 2017 the authors.*

As for intravital inspection, accessibility to deep tissue is desirable. A variety of novel endomicroscopy, such as endoscopic PA imaging [75] and endoscopic optical coherence tomography [76], are emerging. However, these endoscopic modalities are mainly used for in vivo anatomical analysis due to their limited cell contrast [77,78]. Instead, using minimally invasive distal optics provides a promising endomicroscopic approach to help access the deep tissue. For example, Vasquez-Lopez et al. reported a minimally invasive endomicroscopy by embedding a multimode fiber (MMF) in the deep brain of a mouse [17]. In this endomicroscopy, the wavefront modulation enabled by a spatial light modulator was used to perform the 3D imaging of brain tissues through the MMF [79,80]. In this work, the resolution was ~1.27 μm in the lateral direction and ~20.2 μm in the axial direction. The capability of intravital neuron imaging in the deep brain has been demonstrated on a mouse model, as shown in Fig. 11.21. Through tracking the intensity change of the fluorescent Ca^{2+} reporter in the auditory thalamus with the sound stimuli, this system was able to study the neuron dynamics in vivo in the deep brain.

11.6 Conclusion

Fiber-optic-based sensing, manipulation, and imaging techniques for cellular analysis have advanced the fundamental understanding of basic cell biology and led to new diagnostic methods. This chapter summarizes the recent development of fiber-optic devices for bulk-cell analysis, single-cell analysis, and intravital-cell analysis.

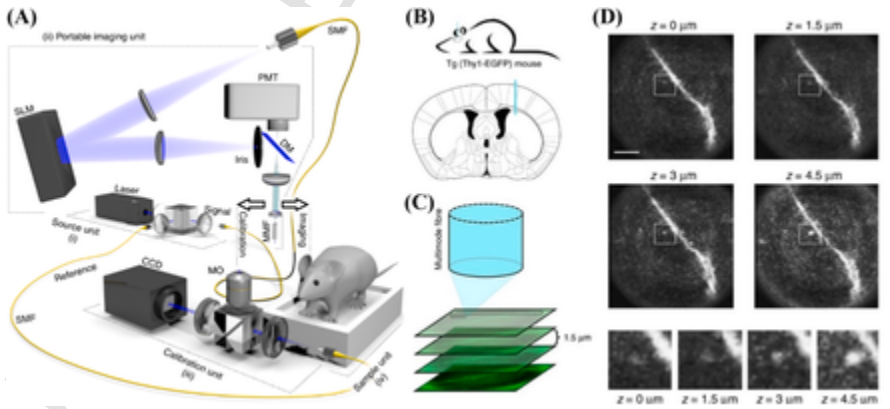

FIGURE 11.21

(A) Schematic of a minimally invasive endomicroscopy system. (B) The placement of an MMF in the mouse brain. (C) Optical 3D deep brain imaging via the MMF using a spatial light modulator. (D) Fluorescent images acquired at different depths in the mouse brain. *MMF*, Multimode fiber.

- *Adapted from* [17]. *© 2018 the authors.*

As for bulk-cell analysis, RI sensing with fiber-optics devices provides a highly sensitive, label-free, and real-time approach for detecting cancer cells, sensing the cell metabolites, and tracking the cellular behaviors. Although great advancement has been made in the sensitivity of fiber-optic-based RI sensors, there are still two challenges in cell detection and cell response monitoring. First, optical fiber is not an ideal platform to enrich the rare target cells due to its limited size. Combining the sensitive cell detection of fiber-optic RI sensors with the flexible analyte processing capability of microfluidic devices maybe a feasible solution. Second, it is challenging for fiber-optic sensors to monitor complex cellular responses involving multiple reactions simultaneously, such as the triggering of several signaling pathways in cells. A rigorous design of the control experiment with an intelligent method is needed to distinguish multiple cellular responses from the collective sensing signals of intracellular RI changes.

As for single-cell analysis, two types of fiber-optic-based devices have been introduced. The first type is based on OFTs for cellular and subcellular manipulations, including cell positioning and sorting, measurements of mechanical properties of cells, and cell microsurgery. OFTs can apply force in the order of pico-Newton and measure the velocity in the range of a few micrometers per second. The second type is for profiling of intracellular biochemical dynamics, such as molecular uptake, oxidative stress events, and apoptosis. These fiber biosensors usually have a sub-micrometer fiber tip, offering label-free and minimally invasive probing of cells without affecting their viability. It is promising to develop fiber-optic devices integrating cellular and subcellular manipulations with biosensing capabilities in the future.

As for intravital-cell analysis, fiber-optic-based in vivo flow cytometry and endomicroscopy have been developed. In vivo flow cytometry provides accurate, rapid, and real-time detection of target cells, such as CTCs, or cell clusters, such as CBCs, in blood vessels. However, it is imperative to further advance in vivo flow cytometry for high throughput. On the other hand, fiber-optics-based endomicroscopy offers cellular resolution and a large field of view to clearly delineate the tissue structures and monitor the activities of living cells in deep tissues. For future clinical use of endomicroscopy, it is desirable to further improve the spatial and temporal resolutions, increase the field of view, and reduce the size to minimize the invasiveness.

Reference

[1] J.R. Heath, et al., Single-cell analysis tools for drug discovery and development, Nat. Rev. Drug Discov. 15 (2016) 204–216.
[2] D. Wang, S. Bodovitz, Single cell analysis: the new frontier in ‘omics', Trends Biotechnol. 28 (2010) 281–290.
[3] C. Caucheteur, et al., Review of plasmonic fiber optic biochemical sensors: improving the limit of detection, Anal. Bioanal. Chem. 407 (2015) 3883–3897.
[4] M. Loyez, et al., Rapid detection of circulating breast cancer cells using a multiresonant optical fiber aptasensor with plasmonic amplification, ACS Sens. 5 (2020) 454–463.

[5] Z. Luo, et al., Ultrasensitive U-shaped fiber optic LSPR cytosensing for label-free and in situ evaluation of cell surface *N*-glycan expression, Sens. Actuators B: Chem. 284 (2019) 582–588.
[6] R. Singh, et al., Etched multicore fiber sensor using copper oxide and gold nanoparticles decorated graphene oxide structure for cancer cells detection, Biosens. Bioelectron. 168 (2020) 112557.
[7] H. Lu, et al., Au-NPs signal amplification ultra-sensitivity optical microfiber interferometric biosensor, Opt. Express 29 (2021) 13937–13948.
[8] F. Xia, et al., Ultra-high sensitivity SPR fiber sensor based on multilayer nanoparticle and Au film coupling enhancement, Measurement 164 (2020) 108083.
[9] Y. Yildizhan, et al., FO-SPR biosensor calibrated with recombinant extracellular vesicles enables specific and sensitive detection directly in complex matrices, J. Extracell. Vesicles 10 (2021) e12059.
[10] S. Liu, et al., Miniaturized optical fiber tweezers for cell separation by optical force, Opt. Lett. 44 (2019) 1868–1871.
[11] V.E. Pera, et al., Diffuse fluorescence fiber probe for in vivo detection of circulating cells, J. Biomed. Opt. 22 (2017) 037004.
[12] X. Tan, et al., In vivo flow cytometry of extremely rare circulating cells, Sci. Rep. 9 (2019) 1–11.
[13] M.A. Juratli, et al., Noninvasive label-free detection of circulating white and red blood clots in deep vessels with a focused photoacoustic probe, Biomed. Opt. Express 9 (2018) 5667–5677.
[14] J. Ahn, et al., In vivo longitudinal cellular imaging of small intestine by side-view endomicroscopy, Biomed. Opt. Express 6 (2015) 3963–3972.
[15] E.J. Jun, et al., In vivo fluorescence microendoscopic monitoring of stent-induced fibroblast cell proliferation in an esophageal mouse model, J. Vasc. Intervent. Radiol. 29 (2018) 1756–1763.
[16] W. Liang, et al., Nonlinear optical endomicroscopy for label-free functional histology in vivo, Light: Sci. Appl. 6 (2017) e17082.
[17] S.A. Vasquez-Lopez, et al., Subcellular spatial resolution achieved for deep-brain imaging in vivo using a minimally invasive multimode fiber, Light: Sci. Appl. 7 (2018) 1–6.
[18] X. Yu, et al., Plasmonic enhanced fluorescence spectroscopy using side-polished microstructured optical fiber, Sens. Actuators B: Chem. 160 (2011) 196–201.
[19] X. Yu, et al., An efficient approach for investigating surface plasmon resonance in asymmetric optical fibers based on birefringence analysis, Opt. Express 18 (2010) 17950–17957.
[20] D.J.J. Hu, H.P. Ho, Recent advances in plasmonic photonic crystal fibers: design, fabrication and applications, Adv. Opt. Photonics 9 (2017) 257–314.
[21] E. Kretschmann, H. Raether, Radiative decay of non radiative surface plasmons excited by light, Z. Für Naturforschung A 23 (1968) 2135–2136.
[22] A. Otto, Excitation of nonradiative surface plasma waves in silver by the method of frustrated total reflection, Z. Für Phys. A Hadron. Nucl. 216 (1968) 398–410.
[23] K.M. Mayer, J.H. Hafner, Localized surface plasmon resonance sensors, Chem. Rev. 111 (2011) 3828–3857.
[24] M. Shabaninezhad, G. Ramakrishna, Theoretical investigation of size, shape, and aspect ratio effect on the LSPR sensitivity of hollow-gold nanoshells, J. Chem. Phys. 150 (2019) 144116.

[25] G.M. Das, et al., Biosensing using SERS active gold nanostructures, Nanomaterials 11 (2021) 2679.
[26] M.A. Badshah, et al., Recent developments in plasmonic nanostructures for metal enhanced fluorescence-based biosensing, Nanomaterials 10 (2020) 1749.
[27] D. Yi, et al., Interrogation technique analyses of a hybrid fiber optic sensor based on SPR and MMI, Opt. Express 28 (2020) 20764–20772.
[28] G. Liang, et al., Fiber optic surface plasmon resonance–based biosensor technique: fabrication, advancement, and application, Crit. Rev. Anal. Chem. 46 (2016) 213–223.
[29] Q. Wu, et al., Singlemode-multimode-singlemode fiber structures for sensing applications—a review, IEEE Sens. J. 21 (2020) 12734–12751.
[30] Y. Yanase, et al., Development of an optical fiber SPR sensor for living cell activation, Biosens. Bioelectron. 25 (2010) 1244–1247.
[31] W. Hong, et al., Nanoscale label-free bioprobes to detect intracellular proteins in single living cells, Sci. Rep. 4 (2014) 1–5.
[32] J. Chen, et al., Single-cell oxidative stress events revealed by a renewable SERS nanotip, ACS Sens. 6 (2021) 1663–1670.
[33] Y. Ying, et al., Recent research progress of optical fiber sensors based on D-shaped structure, Opt. Laser Technol. 90 (2017) 149–157.
[34] A.J.Y. Tan, et al., Trends and applications of U-shaped fiber optic sensors: a review, IEEE Sens. J. 21 (2020) 120–131.
[35] Y. Shevchenko, et al., Surface plasmon resonance fiber sensor for real-time and label-free monitoring of cellular behavior, Biosens. Bioelectron. 56 (2014) 359–367.
[36] D. Li, et al., Label-free fiber nanograting sensor for real-time in situ early monitoring of cellular apoptosis, Adv. Photonics 4 (2022) 016001.
[37] T. Guo, et al., Plasmonic optical fiber-grating immunosensing: a review, Sensors 17 (2017) 2732.
[38] A. Miliou, In-fiber interferometric-based sensors: overview and recent advances, Photonics (2021) 265.
[39] D. Rho, et al., Demonstration of a low-cost and portable optical cavity-based sensor through refractive index measurements, Sensors 19 (2019) 2193.
[40] H. Wu, et al., An ultra-low detection-limit optofluidic biosensor based on all glass Fabry-Perot cavity, Opt. Express 22 (2014) 31977–31983.
[41] W. Yu, et al., Label-free fiber optic biosensor based on thin-core modal interferometer, Sens. Actuators B: Chem. 228 (2016) 322–329.
[42] Y. Li, et al., Immobilized optical fiber microprobe for selective and high sensitive glucose detection, Sens. Actuators B: Chem. 255 (2018) 3004–3010.
[43] X. Li, et al., High-sensitivity Sagnac-interferometer biosensor based on exposed core microstructured optical fiber, Sens. Actuators B: Chem. 269 (2018) 103–109.
[44] G. An, et al., Glucose sensor realized with photonic crystal fiber-based Sagnac interferometer, Opt. Commun. 405 (2017) 143–146.
[45] A. Ashkin, et al., Observation of a single-beam gradient force optical trap for dielectric particles, Opt. Lett. 11 (1986) 288–290.
[46] C.J. Bustamante, et al., Optical tweezers in single-molecule biophysics, Nat. Rev. Methods Prim. 1 (2021) 1–29.
[47] Y. Lou, et al., Optical trapping and manipulation using optical fibers, Adv. Fiber Mater. 1 (2019) 83–100.
[48] J. Chen, et al., Photochemically synthesized silver nanostructures on tapered fiber as plasmonic tweezers for surface enhanced Raman scattering applications, Vacuum 118

(2015) 171–176.
[49] J. Chen, et al., Plasmonic random nanostructures on fiber tip for trapping live cells and colloidal particles, Opt. Lett. 40 (2015) 3926–3929.
[50] G. Pesce, et al., Optical tweezers: theory and practice, Eur. Phys. J. Plus 135 (2020) 1–38.
[51] V.V. Datsyuk, O.R. Pavlyniuk, Maxwell stress on a small dielectric sphere in a dielectric, Phys. Rev. A 91 (2015) 023826.
[52] E.M. Hassan, et al., In vitro selections of mammaglobin A and mammaglobin B aptamers for the recognition of circulating breast tumor cells, Sci. Rep. 7 (2017) 1–18.
[53] M. Willander, et al., Recent progress on growth and device development of ZnO and CuO nanostructures and graphene nanosheets, J. Mater. Chem. 22 (2012).
[54] V. Georgakilas, et al., Noncovalent functionalization of graphene and graphene oxide for energy materials, biosensing, catalytic, and biomedical applications, Chem. Rev. 116 (2016) 5464–5519.
[55] M. Ding, et al., Mesoporous nanospheres functionalized optical microfiber biosensor for low concentration neurotransmitter detection, Opt. Express 24 (2016) 27152–27159.
[56] W. Luo, et al., Recent progress in microfiber-optic sensors, Photonic Sens. 11 (2021) 45–68.
[57] K. L. Cox, et al., Immunoassay methods, in: Assay Guidance Manual [Internet], 2019.
[58] C. A. Janeway Jr, et al., The structure of a typical antibody molecule, in: Immunobiology: The Immune System in Health and Disease, fifth ed., Garland Science, 2001.
[59] S. Ferguson, R. Weissleder, Modeling EV kinetics for use in early cancer detection, Adv. Biosyst. 4 (2020) 1900305.
[60] J. Kitaura, Tuning IgE: IgE-associating molecules and their effects on IgE-dependent mast cell reactions, Cells 10 (2021).
[61] E. Hodzic, Single-cell analysis: Advances and future perspectives, Bosn. J. Basic Med. Sci. 16 (2016) 313.
[62] Y. Li, et al., Non-contact intracellular binding of chloroplasts in vivo, Sci. Rep. 5 (2015) 1–9.
[63] X. Zhao, et al., In situ single-cell surgery and intracellular organelle manipulation via thermoplasmonics combined optical trapping, Nano Lett. (2021).
[64] H. Xin, et al., Escherichia coli-based biophotonic waveguides, Nano Lett. 13 (2013) 3408–3413.
[65] S. Yang, G. Lian, ROS and diseases: role in metabolism and energy supply, Mol. Cell Biochem. 467 (2020) 1–12.
[66] C.T. Madreiter-Sokolowski, et al., Interrelation between ROS and Ca2+ in aging and age-related diseases, Redox Biol. 36 (2020) 101678.
[67] W. Yuan, et al., Optimal operational conditions for supercontinuum-based ultrahigh-resolution endoscopic OCT imaging, Opt. Lett. 41 (2016) 250–253.
[68] W. Yuan, et al., Super-achromatic monolithic microprobe for ultrahigh-resolution endoscopic optical coherence tomography at 800 nm, Nat. Commun. 8 (2017) 1–9.
[69] W. Yuan, et al., Theranostic OCT microneedle for fast ultrahigh-resolution deep-brain imaging and efficient laser ablation in vivo, Sci. Adv. 6 (2020) eaaz9664.
[70] J. Thiboutot, et al., Visualization and validation of the microstructures in the airway wall in vivo using diffractive optical coherence tomography, Acad. Radiol. (2022).
[71] W. Yuan, et al., In vivo assessment of inflammatory bowel disease in rats with ultrahigh-resolution colonoscopic OCT, Biomed. Opt. Express 13 (2022) 2091–2102.

[72] I. Georgakoudi, et al., In vivo flow cytometry: a new method for enumerating circulating cancer cells, Cancer Res. 64 (2004) 5044–5047.
[73] Y. Suo, et al., Advances of in vivo flow cytometry on cancer studies, Cytometry Part A 97 (2020) 15–23.
[74] M.A. Juratli, et al., Real-time label-free embolus detection using in vivo photoacoustic flow cytometry, PLoS One 11 (2016) e0156269.
[75] Y. Li, et al., Advances in endoscopic photoacoustic imaging, in: *Photonics*, 2021, p. 281.
[76] P. Si, et al., Optical microscopy and coherence tomography of cancer in living subjects, Trends Cancer 6 (2020) 205–222.
[77] J. Hu, et al., Gold nanoshells: contrast agents for cell imaging by cardiovascular optical coherence tomography, Nano Res. 11 (2018) 676–685.
[78] J.E. Lemaster, et al., Gadolinium doping enhances the photoacoustic signal of synthetic melanin nanoparticles: a dual modality contrast agent for stem cell imaging, Chem. Mater. 31 (2018) 251–259.
[79] D. Stellinga, et al., Time-of-flight 3D imaging through multimode optical fibers, Science 374 (2021) 1395–1399.
[80] M. Kim, et al., Transmission matrix of a scattering medium and its applications in biophotonics, Opt. Express 23 (2015) 12648–12668.